https://doi.org/10.5194/egusphere-2026-4182
Preprint. Discussion started: 30 July 2026

Brief communication: Ambient-pressure femtosecond laser ablation as a solid-phase sampling method for water ice

Robin Vinther Nielsen[1], Ioanna Bertsia-Kanatouri[1], Kerttu Maria Peensoo[1,†], Simon Alexander Munk Wael Fassel[1], Eirini Malegiannaki[1,‡], and Vasileios Gkinis[1]

[1]Niels Bohr Institute, University of Copenhagen
[†]now at: Second Sun ApS
[‡]now at: Helmholtz Centre for Polar and Marine Research, Alfred Wegener Institute

Correspondence: Vasileios Gkinis (v.gkinis@nbi.ku.dk)

Abstract. High-resolution ice-core analysis requires sampling methods that preserve millimeter to sub-millimeter spatial information. We evaluate ambient-pressure femtosecond laser ablation (fs-LA) as a solid-phase and geometry-tolerant sampling method for water ice under cold, dry laboratory conditions. At 35 μJ and 50 kHz, visible localized craters were produced at all tested exposure times, with mean inner diameters of approximately 87–165 μm. Crater formation was repeatable at a 0.5 mm pitch along 400-position scan paths. The 1 s exposure produced the smallest sampling footprint and largest fraction of craters without visible rims, supporting fs-LA as a platform for future cryospheric analyses.

1 Introduction

High-resolution measurements of ice cores and other stratified ice samples require sampling methods that preserve spatial information at the millimeter to sub-millimeter scale, especially in highly compressed or finely stratified ice where annual layers, impurity bands, melt features, grain-boundary structures, and other markers may occur below the scale accessible by conventional sampling (Jouzel et al., 1997; Casado et al., 2018). Many established ice-core workflows rely on melting the sample before analysis, including continuous flow analysis for chemical impurities (Bigler et al., 2011) and stable water isotopes (Gkinis et al., 2011; Emanuelsson et al., 2015; Jones et al., 2017), as well as discrete sampling for isotope and chemistry measurements (Baker et al., 2002). However, conversion to the liquid phase introduces dispersion, mixing, and loss of the original solid-phase structure, limiting the interpretation of fine-scale stratigraphic features.

Laser ablation (LA), the removal of material from a surface by focused laser irradiation, offers a solid-phase alternative by locally sampling the ice surface without bulk melting. By sampling only a small volume, LA can leave most of the ice section available for visual stratigraphy, microstructural characterization, replicate sampling, or complementary analyses, while providing spatially resolved material for isotopic, chemical, elemental, or stratigraphic analyses.

LA methods have already been applied in ice-core research. LA inductively coupled plasma mass spectrometry has demonstrated sub-millimeter trace-element analysis in ice (Della Lunga et al., 2014), and LA has recently been coupled to cavity ring-down spectroscopy (CRDS) for direct isotope analysis of ice (Malegiannaki et al., 2024). However, existing implementations commonly use nanosecond lasers, enclosed ablation cells, controlled carrier-gas environments, or cryogenic sample

https://doi.org/10.5194/egusphere-2026-4182
Preprint. Discussion started: 30 July 2026

chambers. For example, the recent LA–CRDS measurements used raster scans over 4×4 mm areas in an integrated ablation chamber, giving a 4 mm sampling resolution along the ice-core depth axis. Such requirements can restrict sample geometry and complicate analysis of long or irregularly shaped ice sections.

fs-LA uses ultrashort laser pulses and provides a different interaction regime from nanosecond LA because energy deposition occurs on timescales shorter than characteristic heat diffusion (Chichkov et al., 1996). This is relevant for water ice, a low-melting-temperature dielectric whose response may be influenced by phase changes, optical heterogeneity, and microstructure. Ambient-pressure fs-LA may therefore offer a geometry-tolerant route to localized solid-phase sampling, but its behavior on water ice under practical cold-laboratory conditions remains insufficiently characterized.

Here, we evaluate ambient-pressure fs-LA as a solid-phase sampling method for water ice. The study focuses on crater morphology, reproducibility, visible rim formation, and along-scan consistency under cold, dry laboratory conditions. Rather than validating a specific downstream analytical coupling, the aim is to establish whether fs-LA can provide controlled, localized, and minimally destructive material removal suitable for future high-resolution cryospheric analyses.

2 Experimental setup and methods

A femtosecond laser system (ORIGAMI XPS, NKT Photonics) operating at 1030 nm was used for all experiments. The laser was operated at 35 μJ and 50 kHz in pulse-train mode, with the ice surface held stationary during each exposure. The beam was delivered through a free-space optical path and focused vertically onto the ice surface inside a modified commercial chest-freezer cryochamber operated at ambient pressure, flushed with dry air, and approximately $-20\,^{\circ}$C. A co-axial imaging path allowed post-exposure crater imaging. The effective beam diameter at the sample was approximately 96 μm, giving a nominal peak fluence of approximately $0.97\ \mathrm{J\,cm^{-2}}$ at 35 μJ. Details of the setup, optical layout, beam-diameter estimate, fluence calculation, and exploratory threshold treatment are provided in Appendices A and B.

Synthetic ice was produced from degassed deionized water (Milli-Q) and directionally frozen to reduce bubble content. Samples were cut into 30×30 mm sticks and microtomed before ablation. Ice sections of approximately 30 cm length were mounted on a polycarbonate holder coupled to a motorized linear translation stage that can accommodate sections up to 50 cm long. During ablation, the sample was translated beneath the stationary laser beam, controlled by a combined linear stage and fs-laser Python interface. For the exposure series, discrete ablation sites were produced with a 0.5 mm step size at 1, 2, 4, 8, and 16 s exposure times, with 400 ablation sites per exposure condition. Details of the ice preparation are provided in Appendix C.

Post-exposure crater images were analyzed with a custom Python tool and calibrated using a microscope calibration slide. Each ablation position was classified as analyzable or non-analyzable based on whether the crater boundary could be reliably identified. For analyzable craters, the inner crater diameter D_c was measured; where a surrounding rim or boundary feature was visible, an outer rim diameter D_r was also measured and $R = D_\mathrm{r}/D_\mathrm{c}$ was calculated. Craters without a measurable D_r were classified as no visible rim, while rimmed craters were classified as narrow for $1 < R < 1.8$, intermediate for $1.8 \leq R < 2.8$, and broad for $R \geq 2.8$. These operational classes were chosen as pragmatic bins to summarize visible morphology only and

https://doi.org/10.5194/egusphere-2026-4182
Preprint. Discussion started: 30 July 2026

are not interpreted as direct measurements of melt volume, redeposition, or ablated mass. Physical context for these features is provided in Appendix D.

3 Results

Table 1. Summary of crater visibility, operational morphology classes, and diameter statistics for the 35 μJ exposure series. Each exposure condition consisted of 400 ablation positions. Percentages for no visible rim and rim classes are given relative to visible/analyzable craters. Statistics for R are calculated only for craters with a measurable outer rim. Uncertainties denote one standard deviation.

Exposure (s)	Visible n (%)	Non-analyzable n (%)	No rim n (%)	Narrow n (%)	Intermediate n (%)	Broad n (%)	D_c (μm)	R
1	382 (95.5)	18 (4.5)	245 (64.1)	14 (3.7)	113 (29.6)	10 (2.6)	86.5 ± 13.5	2.22 ± 0.49
2	393 (98.3)	7 (1.8)	135 (34.4)	117 (29.8)	135 (34.4)	6 (1.5)	107.8 ± 19.5	1.90 ± 0.38
4	386 (96.5)	14 (3.5)	77 (19.9)	51 (13.2)	231 (59.8)	27 (7.0)	114.7 ± 14.0	2.18 ± 0.43
8	382 (95.5)	18 (4.5)	23 (6.0)	23 (6.0)	233 (61.0)	103 (27.0)	132.5 ± 18.5	2.54 ± 0.47
16	375 (93.8)	25 (6.2)	98 (26.1)	105 (28.0)	163 (43.5)	9 (2.4)	164.8 ± 18.3	1.98 ± 0.39

Representative crater morphologies are shown in Fig. 1a. The images illustrate the operational image-analysis classes. The along-scan distribution of these classes is shown in Fig. 1b, and the corresponding counts are summarized in Table 1.

Visible craters were recorded under all exposure conditions. Visibility was high across the exposure series, ranging from 93.8 % at 16 s to 98.3 % at 2 s. The 1 s condition had the largest fraction of craters without a visible rim, with 245 of 382 visible craters classified as no-rim craters. The 8 s condition had the largest broad-rim fraction, with 103 of 382 visible craters classified as broad-rim craters.

The inner crater diameter was measured for all visible craters in each exposure sequence (Fig. 2a; Table 1). Mean inner diameter increased overall with exposure time, from $86.5 \pm 13.5\,\mu\text{m}$ at 1 s to $164.8 \pm 18.3\,\mu\text{m}$ at 16 s. The distributions were approximately unimodal and showed overlap between adjacent exposure conditions.

The 2 and 4 s conditions had partly overlapping inner-diameter distributions, with mean inner diameters of $107.8 \pm 19.5\,\mu\text{m}$ and $114.7 \pm 14.0\,\mu\text{m}$, respectively. However, their rim statistics differed: the 2 s condition had similar fractions of no-rim, narrow-rim, and intermediate-rim craters, whereas the 4 s condition was dominated by intermediate-rim craters. The mean rim-to-crater diameter ratio was lowest at 2 s, $R = 1.90 \pm 0.38$, and highest at 8 s, $R = 2.54 \pm 0.47$.

Spatial consistency was evaluated from the sequence of crater diameters along each scan path (Fig. 2b). For each exposure condition, the rolling mean ($n = 15$) of the inner crater diameter remained within a limited range over most of the 400-position sequence. No scan showed a sustained loss of visible crater formation over the full measurement sequence.

The 1 s sequence showed the smallest inner diameters, mostly between approximately 75 and 100 μm, while the 16 s sequence showed the largest diameters, mostly around 155–180 μm. The rim-to-crater diameter ratio also varied along the scan

https://doi.org/10.5194/egusphere-2026-4182
Preprint. Discussion started: 30 July 2026

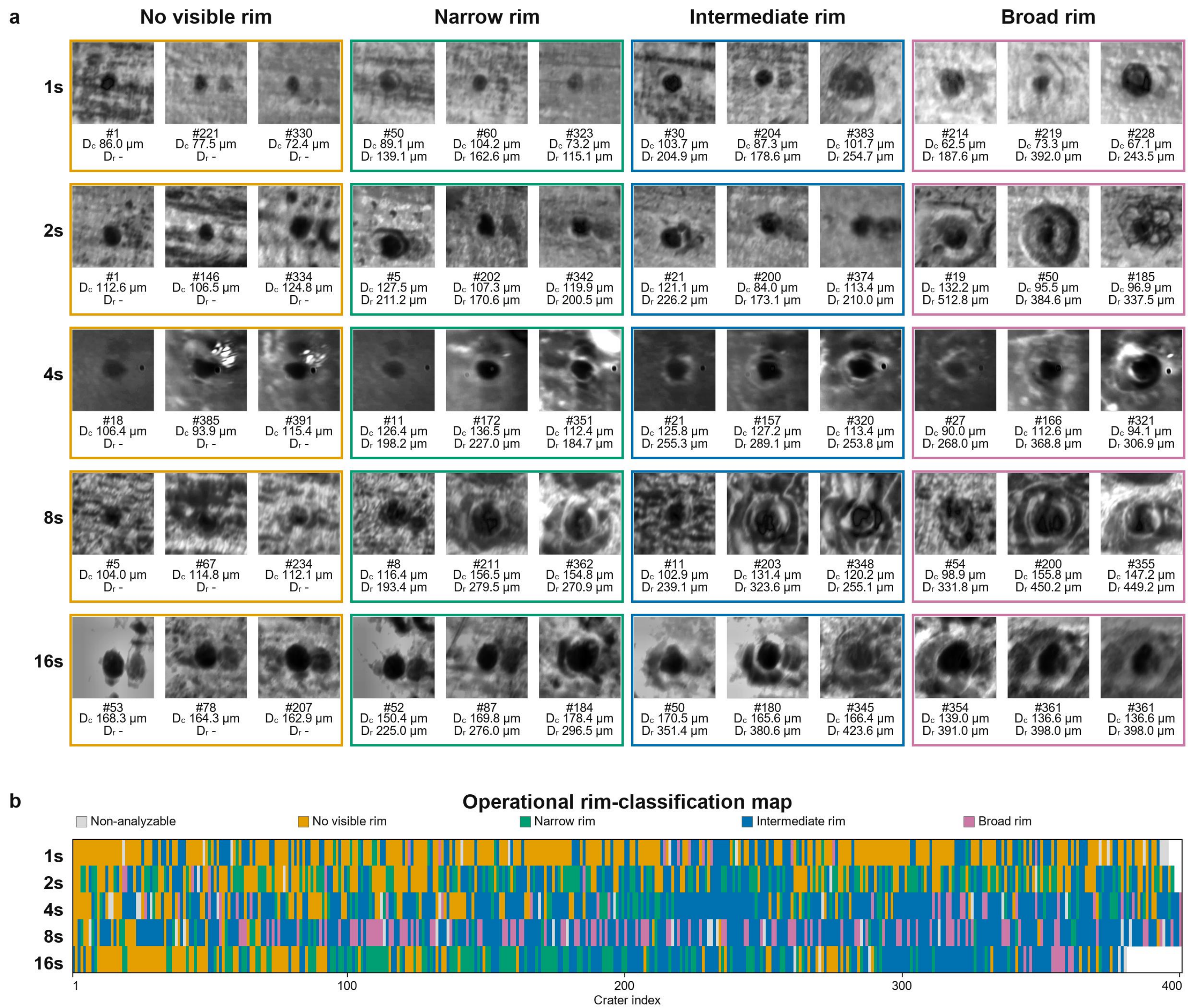

Figure 1. Representative crater morphologies and operational classification for the 35 μJ exposure series. (a) Representative crater morphologies for the operational image-analysis classes used in this study. Rows show exposure times of 1, 2, 4, 8, and 16 s, and columns show craters classified as no visible rim, narrow rim, intermediate rim, and broad rim. Labels below each image indicate the crater index number, inner crater diameter D_c, and outer rim diameter D_r, where available. (b) Operational classification map showing non-analyzable positions, craters without a visible rim, and craters with narrow, intermediate, or broad rims along each scan path. Each scan consisted of 400 ablation positions spaced 0.5 mm apart. The classes are descriptive image-analysis categories and are not interpreted as direct measurements of melt volume, redeposition, or ablated mass.

https://doi.org/10.5194/egusphere-2026-4182
Preprint. Discussion started: 30 July 2026

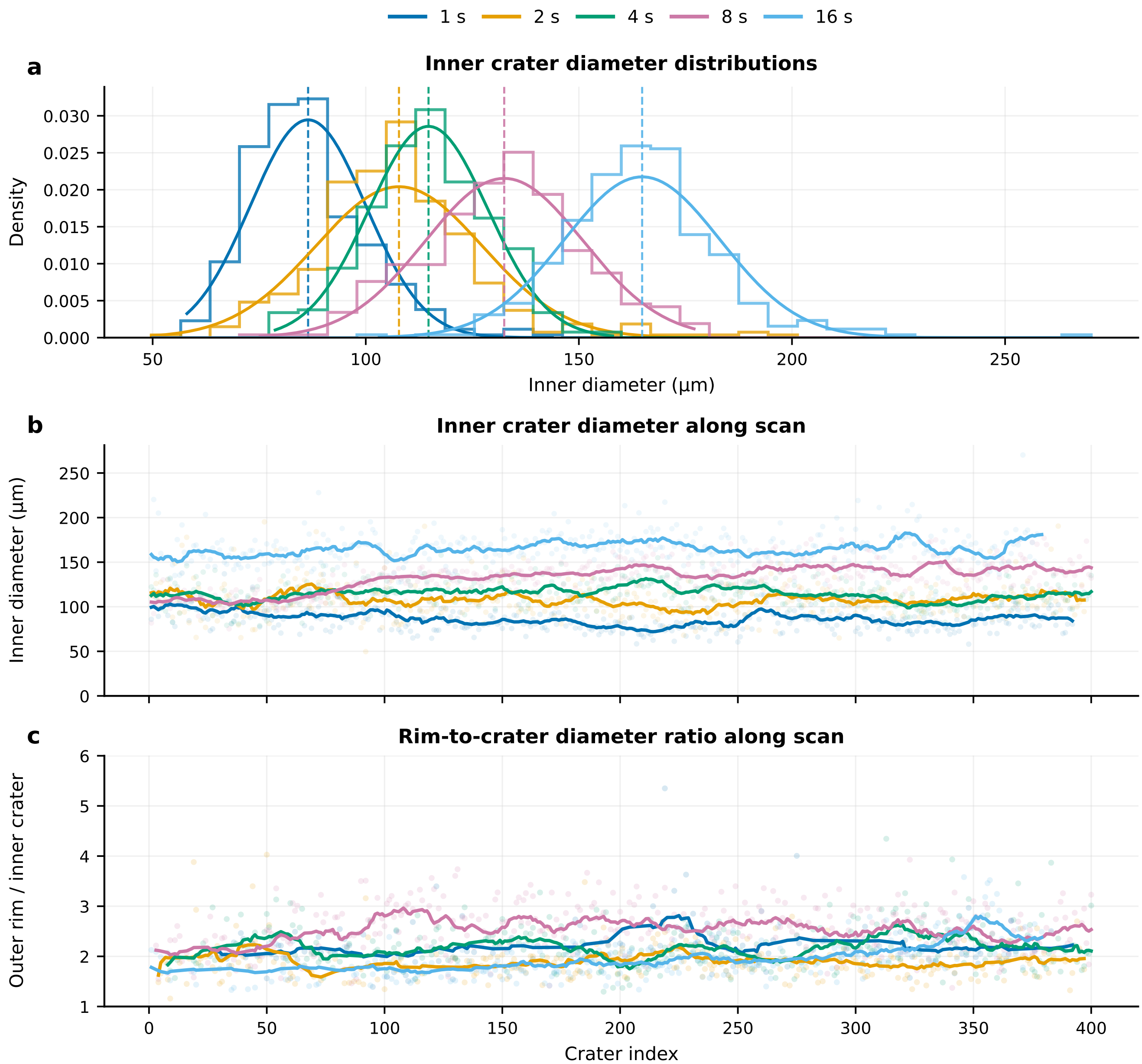

Figure 2. Crater dimensions and along-scan variability for the 35 μJ exposure series. (a) Inner crater diameter distributions for exposure times of 1, 2, 4, 8, and 16 s. Histograms show measured inner diameters, solid curves show Gaussian fits for visual comparison, and dashed vertical lines indicate mean values. (b) Inner crater diameter along each scan path. Points show individual crater measurements, and solid lines show rolling means ($n = 15$). (c) Rim-to-crater diameter ratio along each scan path for craters with a measurable outer rim. Points show individual crater measurements, and solid lines show rolling means ($n = 15$).

https://doi.org/10.5194/egusphere-2026-4182
Preprint. Discussion started: 30 July 2026

path (Fig. 2c), with the highest mean value occurring in the 8 s sequence. Overall, repeated spatially localized craters were produced at a 0.5 mm pitch under all tested exposure conditions.

4 Discussion

The results show that ambient-pressure fs-LA can produce localized and repeatable material removal from water ice under cold-laboratory conditions. The 0.5 mm pitch exceeded the measured inner crater diameters for all exposure conditions, indicating that the inner sampling footprints could be placed without overlap, although visible rim features could extend farther. Crater formation remained broadly stable along the scan paths.

Crater diameter alone was not sufficient to describe sampling quality. The 2 and 4 s conditions had partly overlapping inner-diameter distributions but different rim statistics, while the 8 s condition showed the largest mean rim-to-crater diameter ratio and the largest broad-rim fraction. Among the tested conditions, the 1 s exposure appears to be the best candidate for clean sampling because it produced the smallest mean inner diameter and the largest fraction of craters without a visible rim. The increase in inner crater diameter with exposure time was not linear, which is consistent with multi-pulse threshold and saturating-incubation considerations, summarized in Appendix B. Visible rim morphology and the physical context for boundary feature formation are discussed in Appendix D.

The measured crater dimensions and scan geometry indicate that fs-LA can provide sub-millimeter positioning of the sampling footprint in water ice, which is relevant where cryospheric stratigraphic features may be thinner than the effective resolution of melt-based or discrete sampling approaches. The stationary-beam and translating-sample geometry is compatible with extended ice sections and does not require enclosure in a small ablation chamber. Because only localized regions are sampled, most of the ice section remains available for visual stratigraphy, microstructural analysis, replicate sampling, or complementary measurements. The ablated material could in principle be coupled to isotopic, chemical, elemental, or stratigraphic analyses; CRDS-based isotope analysis is one example, but not the only possible analytical pathway.

The present experiments used synthetic ice produced from degassed Milli-Q water and directionally frozen to reduce bubble content. This provided a controlled material for evaluating the laser–ice interaction, but does not capture the full variability of natural ice-core samples, including stratigraphic layering, variable bubble content, grain structure, fractures, and spatially varying optical properties. The study evaluates morphology only: ablated mass, material yield, transport efficiency, and the isotopic or chemical fidelity of the ablated material were not assessed. Future work should therefore test natural ice and validate downstream couplings separately for each measurement type.

5 Conclusions

Ambient-pressure fs-LA was evaluated as a solid-phase sampling method for water ice under cold, dry laboratory conditions. Visible, spatially localized craters were produced at all tested exposure times, with mean inner diameters of approximately 87–165 μm and repeatable crater formation at a 0.5 mm pitch along 400-position scan paths. Rim expression varied between

https://doi.org/10.5194/egusphere-2026-4182
Preprint. Discussion started: 30 July 2026

exposure conditions, with the 1 s exposure producing the smallest sampling footprint and the largest fraction of craters without a visible rim. These results indicate that fs-LA may provide a geometry-tolerant and minimally destructive sampling platform for future high-resolution cryospheric analyses, although ablated mass, transport efficiency, and analytical fidelity must be validated for specific downstream measurements.

Appendix A: Detailed optical layout and ablation setup

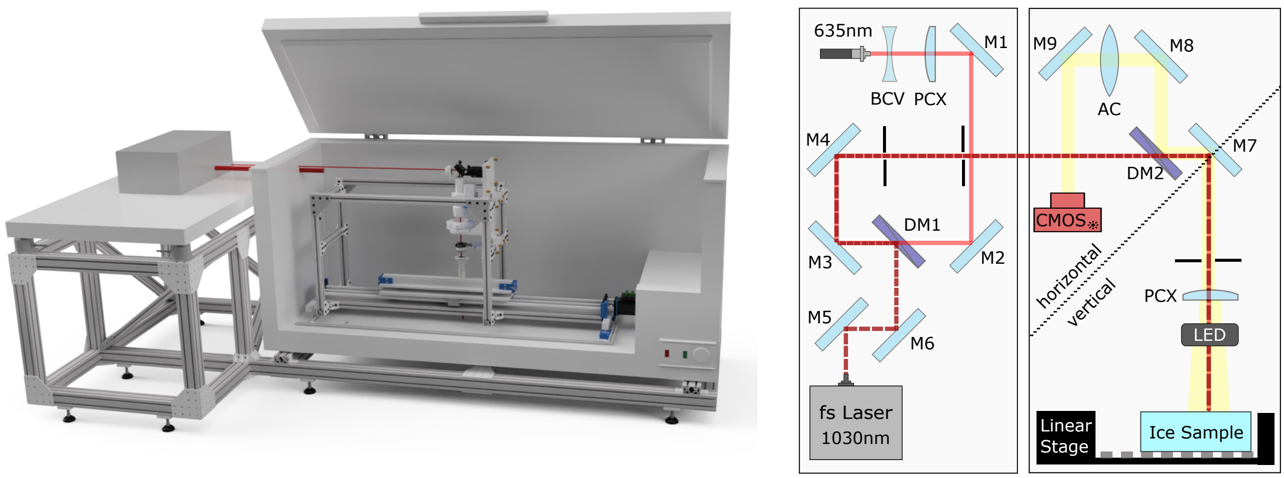

(a) (b)

Figure A1. Ablation setup and optical layout. (a) Rendering of the ambient-pressure fs-LA setup. The laser is delivered from the optical table into a modified chest-freezer cryochamber, where the beam is focused onto ice samples mounted on a motorized linear stage. (b) Detailed optical layout of the femtosecond laser delivery, visible alignment beam, and in situ imaging system. The femtosecond beam at 1030 nm was co-aligned with a 635 nm visible alignment beam before entering the cryochamber. A shared-axis imaging path enabled observation of the ablation site during and after laser exposure.

The optical system was designed to provide co-aligned femtosecond laser delivery and in situ imaging of the sample using a shared optical axis (Fig. A1a,b). The femtosecond laser beam was delivered through a free-space optical path into a modified domestic chest-freezer cryochamber operated at ambient pressure. A $4f$ relay configuration inside the cryochamber enabled imaging of the ablation site onto a CMOS camera. A visible alignment beam was co-propagated with the femtosecond beam to facilitate alignment of the optical path before ablation. The internal surface was covered with black aluminum foil to reduce stray light during imaging. Optical component identifiers in parentheses refer to Thorlabs catalogue part numbers.

The 635 nm alignment laser (PL202) was coupled into the optical path and routed using two alignment mirrors (M1, M2; BB1-E02) mounted in kinematic mirror mounts. The alignment beam was expanded using a Galilean telescope consisting of a plano-convex lens (LA4725-A-ML, $f = 7.5$ mm) and a bi-concave lens (LD2297-A, $f = -25$ mm). This enabled adjustment of the alignment-beam diameter and divergence, improving beam centering at the target plane.

https://doi.org/10.5194/egusphere-2026-4182
Preprint. Discussion started: 30 July 2026

The femtosecond beam was directed along a separate optical path using two silver mirrors (M5, M6; PF10-03-P01). These mirrors delivered the beam to a dichroic mirror (DMSP650), where the femtosecond beam was combined with the visible alignment beam. The dichroic was configured to transmit the 1030 nm femtosecond beam and reflect the 635 nm alignment beam. After combination, two additional protected silver mirrors (M3, M4; PF10-03-P01) were used to adjust the co-aligned beam path.

The alignment of the beam path into the cryochamber was defined using two pinholes (P1, P2; IDA20/M). These served as reference points for centering the co-aligned beam before it entered the chamber. The beam entered through an optical access port and was redirected vertically downward by a protected silver mirror (M7; PF10-03-P01) toward the sample surface. The cumulative dispersion introduced by the external optical path was not independently characterized and may have contributed to pulse broadening at the sample.

Focusing of the femtosecond beam onto the sample was achieved using a plano-convex lens (LA4924-B) with a focal length of 175 mm. The lens was mounted in a piezo-actuated mount (PD1FM + PD1/M), allowing fine adjustment of the focal position. The focal length provided a working distance suitable for the sample geometries used in this study. An additional pinhole (P3; IDA20/M) positioned before the focusing lens was used as an alignment reference before focusing.

The focusing lens also served as the first element of the imaging system. Together with an achromatic doublet (ACT508-500-B, $f = 500\,\mathrm{mm}$), it formed a $4f$ relay that imaged the sample plane onto a CMOS camera (CS165MU1) guided by mirrors M8 and M9 (PF10-03-P01). The nominal magnification of the imaging system was $M = f_2/f_1 \approx 2.9$, based on focal lengths of 175 and 500 mm. The effective magnification was determined experimentally using a microscope calibration slide under the same optical configuration used for crater imaging.

Illumination of the sample was provided by a white LED (LEDWR40) positioned above the sample region. A dichroic mirror (DMLP950) located inside the cryochamber was used to separate the laser and imaging paths. The dichroic transmitted the near-infrared femtosecond beam while reflecting visible illumination and scattered light from the sample toward the CMOS camera. This configuration enabled in situ observation of the ablation site while maintaining a shared optical axis for laser delivery and imaging.

Appendix B: Fluence and incubation context

The effective beam diameter at the sample was estimated using an infrared-sensitive beam profiling card at low pulse energy ($\sim 0.5\,\mu$J). Because the card response is threshold-based, the measured diameter should be interpreted as an effective interaction diameter rather than a strict 1/e^2 beam diameter. The effective beam diameter was measured to be approximately 96 μm.

Assuming a Gaussian spatial profile, the nominal peak fluence F was estimated as

$$F = \frac{2E}{\pi w_0^2}, \tag{B1}$$

where E is the pulse energy and w_0 is the effective beam radius at the sample surface (Liu, 1982). With $E = 35\,\mu$J and $w_0 \approx 48\,\mu$m, this gives $F \approx 0.97\ \mathrm{J\,cm^{-2}}$.

https://doi.org/10.5194/egusphere-2026-4182
Preprint. Discussion started: 30 July 2026

This value should be regarded as a nominal experimental fluence. The main sources of uncertainty are the effective beam-diameter estimate, possible deviations from an ideal Gaussian profile, and uncharacterized pulse broadening in the external optical path. The uncertainty in the fluence estimate is assumed to be on the order of 20–30 %.

For water ice under multi-pulse femtosecond irradiation, a uniquely defined ablation threshold is difficult to establish. Ice is a low-melting-temperature dielectric, and laser energy deposition can lead to a gradual transition from surface modification to material removal through melting, refreezing, vaporization, redeposition, and evolving surface morphology. In addition, the experiments involved large numbers of pulses per ablation site: at 50 kHz, exposure times of 1, 2, 4, 8, and 16 s correspond to approximately 5×10^4, 1×10^5, 2×10^5, 4×10^5, and 8×10^5 pulses per site, respectively.

As an exploratory framework, crater diameters can be related to an effective threshold fluence using the Gaussian threshold method of Liu (1982). For a Gaussian beam, the squared crater diameter scales with the logarithm of the ratio between applied fluence and effective threshold fluence. This is relevant here because crater diameter is not expected to increase linearly with exposure time once the beam center is above threshold. Repeated irradiation can also reduce the effective damage or ablation threshold through incubation processes (Rosenfeld et al., 1999; Ashkenasi et al., 1999). Longer exposures therefore correspond to larger pulse numbers and evolving surface conditions, not independent single-pulse events. These considerations provide context for the observed non-linear exposure-time dependence of crater diameter.

A commonly used description is a power-law decrease in threshold with pulse number,

$$F_{\mathrm{th}}(N) = F_{\mathrm{th}}(1)\, N^{\xi-1}, \tag{B2}$$

where $F_{\mathrm{th}}(1)$ is the inferred single-pulse threshold, N is the number of pulses, and ξ is the incubation coefficient. In this formulation, incubation-driven threshold reduction corresponds to $\xi < 1$, while $\xi = 1$ indicates no change in threshold with pulse number.

An alternative description allows the threshold to approach a finite asymptotic value,

$$F_{\mathrm{th}}(N) = F_{\mathrm{th},\infty} + [F_{\mathrm{th}}(1) - F_{\mathrm{th},\infty}] \exp[-k(N-1)], \tag{B3}$$

where $F_{\mathrm{th},\infty}$ is the asymptotic threshold and k is a rate parameter (Rosenfeld et al., 1999; Ashkenasi et al., 1999; Palo et al., 2022).

These models are useful only as phenomenological descriptions of crater-growth trends under repeated irradiation. They can account for non-linear crater growth with increasing pulse number, as observed in the exposure series, but the fitted parameters should not be interpreted as intrinsic optical or thermophysical constants of ice. Interpreting them as material constants would require a coupled model of heat accumulation, phase change, and evolving surface morphology.

Appendix C: Synthetic ice preparation

Synthetic ice was used to provide homogeneous, low-bubble samples for reproducible fs-LA experiments. The ice was produced from Milli-Q water. Before freezing, the water was heated to about $40\,^{\circ}\mathrm{C}$, and then degassed using a membrane pump to reduce dissolved gases and limit bubble formation during solidification.

https://doi.org/10.5194/egusphere-2026-4182
Preprint. Discussion started: 30 July 2026

Directional freezing was used to further reduce bubble inclusion in the bulk ice. The water was frozen from the bottom upward using a vertically translating heating jacket. During freezing, the heating jacket was gradually lifted over ∼60 hours along the sample using a stepper-motor-driven translation system. This procedure promoted upward migration of residual gases during solidification, producing a lower-bubble bulk region beneath the gas-enriched upper part of the sample.

After freezing, the cylindrical ice sample was sectioned to remove the upper region where residual gases and bubbles were concentrated. These initial cuts were made perpendicular to the cylinder axis and were separate from the cuts used to shape the final ablation samples. The remaining low-bubble ice was then cut into sticks with cross sections of 30×30 mm. Samples were cut along the cylinder axis to maintain consistent material properties between specimens.

Before ablation, the exposed sample surface was prepared with a microtome to produce a flat and smooth surface. This reduced local variations in focus and incidence angle during laser exposure. Prepared samples were stored in sealed plastic bags when not actively measured, both to limit sublimation and to prevent condensation during handling and transfer outside the cryochamber.

The use of synthetic ice was intended to isolate the laser–ice interaction under controlled conditions. Natural ice may contain bubbles, dust, salts, grain boundaries, fractures, and spatially variable optical properties that can influence ablation behavior. Extension of the method to natural ice-core material therefore requires additional characterization.

Appendix D: Rim formation: physical context and energy considerations

The rim classifications used in this study are operational image-analysis classes based on visible crater morphology and the ratio $R = D_\mathrm{r}/D_\mathrm{c}$. Peripheral features around LA sites are commonly discussed in the literature as recast material, redeposited debris, or heat-affected zones (Chichkov et al., 1996; Gao et al., 2023). The analogy is useful for interpretation, but water ice differs from typical ablation targets such as metals or glass because it can undergo melting, refreezing, sublimation, condensation, and redeposition over closely coupled timescales. Local ice properties including bubbles, grain structure, surface roughness, and optical heterogeneity may further affect energy deposition and image contrast. The rim classes therefore describe the visible spatial extent of boundary features rather than identifying their physical composition.

Time-resolved images show the formation of a visible crater rim during exposure. In the example in Fig. D1, a rim-like boundary is already present by approximately 0.15 s, and the apparent inner crater diameter increases between approximately 1.35 and 2.45 s. By approximately 4.45 s the rim appears more irregular, after which little further visible morphological change is observed. This indicates that rim formation begins early during irradiation and that subsequent exposure modifies both the inner crater and the surrounding boundary feature. The image sequence does not, by itself, determine whether the rim consists of refrozen melt, redeposited material, condensed vapor, roughened ice, or an optical-contrast feature.

A simple energy-scale calculation provides context for the size of the observed features. The energy required to warm ice from $-20\,^\circ$C to the melting point and melt it was estimated as

$$q_\mathrm{melt} = c_p \Delta T + L_f \approx 3.7 \times 10^5 \ \mathrm{J\,kg^{-1}},$$

https://doi.org/10.5194/egusphere-2026-4182
Preprint. Discussion started: 30 July 2026

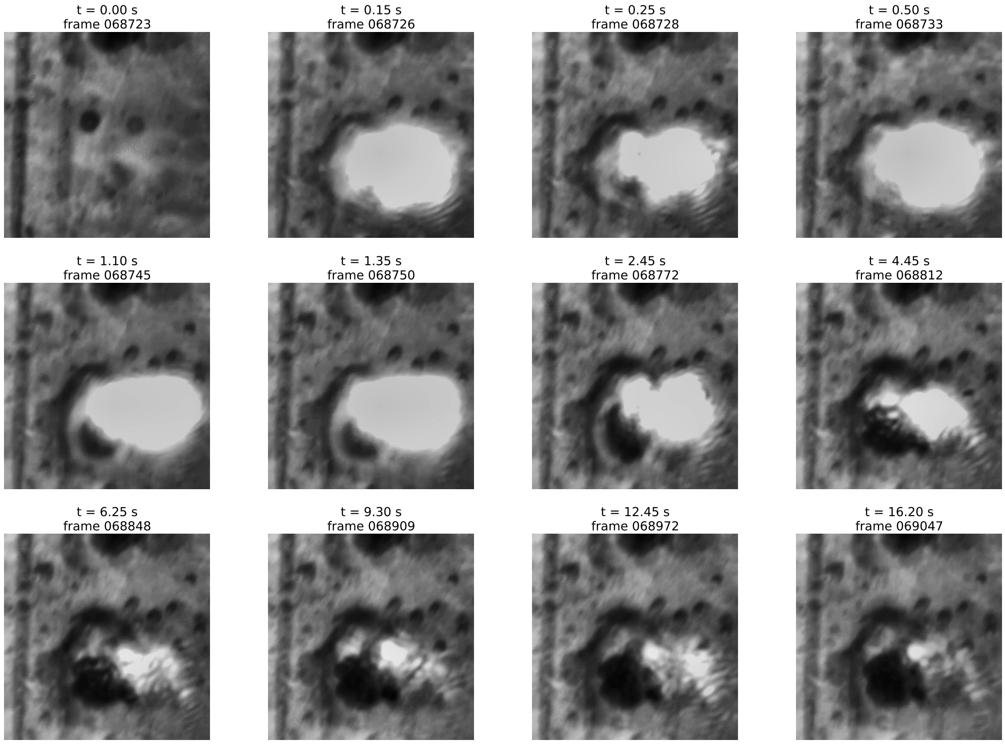

Figure D1. Time-resolved image sequence showing the evolution of a representative ablation site during 16 s exposure. A visible rim-like boundary is present shortly after the start of irradiation, while the apparent inner crater diameter and rim morphology evolve during the first several seconds.

where $c_p \approx 2.0\ \mathrm{kJ\,kg^{-1}\,K^{-1}}$ is the specific isobaric heat capacity of ice, $\Delta T \approx 20\,\mathrm{K}$ is the temperature increase, and $L_f \approx 333.5\ \mathrm{kJ\,kg^{-1}}$ is the latent heat of fusion (Feistel and Wagner, 2006). At 1030 nm, the absorption coefficient for ice is reported as $\alpha = 28.427\ \mathrm{m^{-1}}$, based on the optical constants of Warren and Brandt (2008). For a characteristic path length equal to the 16 s mean inner crater diameter, $d = 164.8\,\mu\mathrm{m}$, the one-pass absorbed fraction is

$$f_{\mathrm{abs}} = 1 - \exp(-\alpha d) \approx 4.7 \times 10^{-3}.$$

Over a 16 s exposure at 50 kHz and 35 μJ per pulse, the incident energy is 28 J, giving an absorbed-energy equivalent of approximately 0.13 J under this one-pass estimate. If used only to warm and melt ice, this energy corresponds to approximately 0.34 mg of ice, or to an equivalent cylindrical depth of approximately 1.8 cm for a diameter of 164.8 μm and ice density $\rho \approx 917\ \mathrm{kg\,m^{-3}}$. This is not a predicted crater depth, because reflection, scattering, heat conduction, vaporization or plasma formation, material ejection, evolving crater geometry, and changing absorption all affect energy partitioning during repeated-pulse exposure. It does, however, show that even a one-pass absorption estimate gives an energy scale large enough for phase change to be relevant, while also emphasizing that the actual crater geometry depends on energy partitioning during repeated-pulse exposure.

This comparison supports interpreting the visible rims as products of coupled material-removal and surface-modification processes, including redeposition of ejected material, displacement and refreezing of transient melt, condensation on the surrounding cold surface, and roughening-induced optical contrast. These processes are also relevant for future isotope or chemical applications, because phase changes, vapor transport, condensation, or redeposition could affect the composition of material delivered to a downstream analyzer.

Data availability. Supporting video and crater-annotation data for this study are available from Zenodo at https://doi.org/10.5281/zenodo.21099024 (Nielsen et al., 2026). The archive documents the 35 μJ fs-LA exposure series on water ice and includes live ablation videos, post-ablation crater-scan videos, and manually annotated crater-analysis CSV files for exposure durations of 1, 2, 4, 8, and 16 s. The archive also includes a README, a CSV column data dictionary, a file manifest, and SHA-256 checksums.

Code availability. The crater-image analysis code used in this study is available at https://github.com/MarsRob/LA_crater_analyzer.

Author contributions. RVN, IBK, KMP, SAMW, EM, and VG contributed to the conception of the study, experimental development, data interpretation, and manuscript revision. RVN performed the crater-image analysis and prepared the initial manuscript draft. All authors reviewed and approved the final manuscript.

Competing interests. The authors declare that they have no conflict of interest.

Acknowledgements. This work was supported by the isoDEEPICE project funded by Independent Research Fund Denmark (Danmarks Frie Forskningsfond, DFF). The authors thank the Physics of Ice and Climate section at the Niels Bohr Institute, University of Copenhagen, for laboratory support and discussions. AI-based writing assistance tools were used for language editing, structural revision, and consistency checks. The authors reviewed and approved the final manuscript and are responsible for its scientific content.

https://doi.org/10.5194/egusphere-2026-4182
Preprint. Discussion started: 30 July 2026

References

Ashkenasi, D., Lorenz, M., Stoian, R., and Rosenfeld, A.: Surface damage threshold and structuring of dielectrics using femtosecond laser pulses: the role of incubation, Applied Surface Science, 150, 101–106, 1999.

Baker, L., Franchi, I. A., Maynard, J., Wright, I. P., and Pillinger, C. T.: A technique for the determination of O-18/O-16 and O-17/O-16 isotopic ratios in water from small liquid and solid samples, Analytical Chemistry, 74, 1665–1673, https://doi.org/10.1021/ac010509s, 2002.

Bigler, M., Svensson, A., Kettner, E., Vallelonga, P., Nielsen, M. E., and Steffensen, J. P.: Optimization of High-Resolution Continuous Flow Analysis for Transient Climate Signals in Ice Cores, Environmental Science & Technology, 45, 4483–4489, https://doi.org/10.1021/es200118j, 2011.

Casado, M., Landais, A., Picard, G., Munch, T., Laepple, T., Stenni, B., Dreossi, G., Ekaykin, A., Arnaud, L., Genthon, C., Touzeau, A., Masson-Delmotte, V., and Jouzel, J.: Archival processes of the water stable isotope signal in East Antarctic ice cores, The Cryosphere, 12, 1745–1766, https://www.the-cryosphere.net/12/1745/2018/, 2018.

Chichkov, B. N., Momma, C., Nolte, S., Alvensleben, F., and Tünnermann, A.: Femtosecond, picosecond and nanosecond laser ablation of solids, Applied Physics A Materials Science & Processing, 63, 109–115, https://doi.org/10.1007/bf01567637, 1996.

Della Lunga, D., Muller, W., Rasmussen, S. O., and Svensson, A.: Location of cation impurities in NGRIP deep ice revealed by cryo-cell UV-laser-ablation ICPMS, Journal of Glaciology, 60, 970–988, https://doi.org/10.3189/2014JoG13J199, 2014.

Emanuelsson, B. D., Baisden, W. T., Bertler, N. A. N., Keller, E. D., and Gkinis, V.: High-resolution continuous-flow analysis setup for water isotopic measurement from ice cores using laser spectroscopy, Atmos. Meas. Tech., 8, 2869–2883, http://www.atmos-meas-tech.net/8/2869/2015/, 2015.

Feistel, R. and Wagner, W.: A New Equation of State for H2O Ice Ih, Journal of Physical and Chemical Reference Data, 35, 1021–1047, https://doi.org/10.1063/1.2183324, 2006.

Gao, W., Zheng, K., Liao, Y., Du, H., Liu, C., Ye, C., Liu, K., Xie, S., Chen, C., Chen, J., Peng, Y., and Leng, Y.: High-Quality Femtosecond Laser Surface Micro/Nano-Structuring Assisted by a Thin Frost Layer, Advanced Materials Interfaces, 10, 2201 924, https://doi.org/10.1002/admi.202201924, 2023.

Gkinis, V., Popp, T. J., Blunier, T., Bigler, M., Schupbach, S., Kettner, E., and Johnsen, S. J.: Water isotopic ratios from a continuously melted ice core sample, Atmospheric Measurement Techniques, 4, 2531–2542, https://doi.org/10.5194/amt-4-2531-2011, 2011.

Jones, T. R., White, J. W. C., Steig, E. J., Vaughn, B. H., Morris, V., Gkinis, V., Markle, B. R., and Schoenemann, S. W.: Improved methodologies for continuous-flow analysis of stable water isotopes in ice cores, Atmos. Meas. Tech., 10, 617–632, http://www.atmos-meas-tech.net/10/617/2017/, 2017.

Jouzel, J., Alley, R. B., Cuffey, K. M., Dansgaard, W., Grootes, P., Hoffmann, G., Johnsen, S. J., Koster, R. D., Peel, D., Shuman, C. A., Stievenard, M., Stuiver, M., and White, J.: Validity of the temperature reconstruction from water isotopes in ice cores, Journal Of Geophysical Research-Oceans, 102, 26 471–26 487, 1997.

Liu, J. M.: Simple technique for measurements of pulsed Gaussian-beam spot sizes, Optics Letters, 7, 196, https://doi.org/10.1364/ol.7.000196, 1982.

Malegiannaki, E., Bohleber, P., Zannoni, D., Stremtan, C., Petteni, A., Stenni, B., Barbante, C., Vinther, B. M., and Gkinis, V.: Towards high-resolution water isotope analysis in ice cores using laser ablation - cavity ring-down spectroscopy, Analyst, 149, 5843–5855, https://doi.org/10.1039/D4AN01054J, 2024.

https://doi.org/10.5194/egusphere-2026-4182
Preprint. Discussion started: 30 July 2026

Nielsen, R. V., Bertsia-Kanatouri, I., Peensoo, K. M., Fassel, S. A. M. W., Malegiannaki, E., and Gkinis, V.: Supporting data for: Ambient-pressure femtosecond laser ablation as a solid-phase sampling method for water ice, https://doi.org/10.5281/zenodo.21099024, 2026.

Palo, R. D., Volpe, A., Gaudiuso, C., Patimisco, P., Spagnolo, V., and Ancona, A.: Threshold fluence and incubation during multi-pulse ultrafast laser ablation of quartz, Opt. Express, 30, 44 908–44 917, https://doi.org/10.1364/OE.475592, 2022.

Rosenfeld, A., Lorenz, M., Stoian, R., and Ashkenasi, D.: Ultrashort-laser-pulse damage threshold of transparent materials and the role of incubation, Applied Physics A, 69, S373–S376, 1999.

Warren, S. G. and Brandt, R. E.: Optical constants of ice from the ultraviolet to the microwave: A revised compilation, J. Geophys. Res., 113, https://doi.org/10.1029/2007JD009744, 2008.